Quantitative impacts of induction heating power on refractory erosion and inclusion behaviour in tundishes

by M. Hao[1], Y. Yin[1], B. Yang[1], L. Wang[1]

Affiliation:
1 School of Materials and Metallurgy, University of Science and Technology Liaoning, PR China

Correspondence to:
B. Yang

Email:
yang583766560@163.com

Dates:
Received: 2 Jul. 2025
Revised: Feb. 2026
Accepted: 7 Feb. 2026
Published: May 2026

How to cite:
Hao, M., Yin, Y., Yang, B., Wang, L. 2026. Quantitative impacts of induction heating power on refractory erosion and inclusion behaviour in tundishes. *Journal of the Southern African Institute of Mining and Metallurgy,* vol. 126, no. 5, pp. 297–308

DOI ID:
https://doi.org/10.17159/2411-9717/3762/2026

ORCiD:
M. Hao
https://orcid.org/0009-0002-0049-1615
Y. Yin
https://orcid.org/0009-0008-4784-3634
B. Yang
https://orcid.org/0000-0001-5987-5790
L. Wang
https://orcid.org/0009-0000-0017-4316

Abstract

This study established a coupled fluid-electromagnetic numerical model to systematically analyzse the effects of molten steel flow, inclusion transport, and temperature gradients on refractory erosion behaviour within an induction-heated tundish. The results demonstrate that increased induction heating power significantly exacerbates both flow-induced erosion and magneto-thermal corrosion of the refractory lining in the channel region. The erosion rate exhibits a linear increase with power, while the wear coefficient follows a power-law relationship. Concurrently, a higher power level intensifies the inclusion collision source term by a factor of ten, substantially promoting inclusion collision, growth, and removal (increasing the removal rate by 14.86%). However, this also leads to a 51.3% reduction in the outlet inclusion particle size. This research provides a quantitative basis for balancing metallurgical benefits (temperature control and improved steel cleanliness) with the longevity-oriented design of refractory linings.

Keywords

induction-heated tundish, refractory erosion, inclusion removal, multi-physical field simulation

Introduction

The tundish is an essential buffer in the continuous casting process, linking ladles to molds. It is widely recognised that the flow characteristics of liquid steel in the tundish critically influence steel purity (Wei et al., 2012; Sheng, 2022; Zhao et al., 2021). To enhance flow dynamics and support the removal of inclusions, flow modification devices such as weirs, dams, and turbulence inhibitors are implemented to promote fluidity. Nonetheless, unsuitable superheat levels of the molten steel can adversely affect billet quality and the operation of casting machines, particularly in low superheat casting scenarios (Xing et al., 2018; Tang et al., 2021; Yong et al., 2020; Xin et al., 2014). Channel-type electromagnetic induction heating tundish (IHT) technology emerges as an innovative solution, enabling consistent-temperature pouring of low-superheat molten steel and facilitating the elimination of non-metallic inclusions (Ghojel, Ibrahim, 2004; Yang et al., 2022). With the continuous advancement in casting technologies and escalating steel quality standards, tundish electromagnetic induction heating technology is progressively evolving to meet these demands (Pan et al., 2022; Bao, Wang, 2021).

The channel-type induction heating tundish represents a novel advancement in the metallurgical field, designed to elevate the pouring temperature of metals, enhance fluidity, and concurrently remove inclusions. Based on electromagnetic induction principles, this technology utilises a tundish—a sizable vessel—to facilitate molten steel transfer and maintain thermal energy during continuous casting. Research predominantly explores the magnetic field characteristics, fluid dynamics, thermal transfer, and inclusion behaviour. Key attributes of the magnetic field include concentrated strength within the channel and an inherent asymmetry, while the flow field is characterised by the altered trajectories influenced by magnetic forces. Thermal dynamics hinge on Joule heating, and inclusion management benefits from heightened collision rates alongside an effective exclusion process. The system encompasses channel induction and plasma heating modalities. Compared to other methods, the channel-type induction heating approach offers superior heating efficiency, user-friendliness, minimal environmental footprint, economic advantages, and an enhancement in metal quality.

The complex dynamics of molten steel flow within a tundish, where an electromagnetic field generates heat, are known to induce significant wear on the refractory lining. Additionally, slag impregnation—which hinges on chemical composition and melting temperature—exacerbates this degradation (Blond et al., 2007; Lian et al., 2018; Rovnushkin et al., 2005). A deeper comprehension of refractory wear during the tundish casting process is crucial for extending the lining's service life. Practical experiments within an actual tundish offer the most direct method for investigating refractory wear. However, measurement constraints and the intense conditions of the casting process often result in a lack of comprehensive data. It is particularly difficult to accurately assess the molten steel flow pattern, inclusion dynamics, electromagnetic heating, and the variations at the slag-steel interface. Such conditions also accentuate chemical corrosion from metallurgical melts, especially molten slag (Tang et al., 2021; Yong et al., 2020).

Erosion-corrosion synergy accelerates the deterioration of the tundish refractory liner, leading to the presence of exogenous inclusions that compromise the cleanliness of molten steel and the mechanical properties of the final steel product. Tundish refractory wall wear is a pivotal concern that affects sequence life. It has been established that this wear can result from thermal, chemical, or mechanical stresses (Crudu et al.,1998). Specifically, the flow of molten steel alone can cause erosion of the refractory lining, and this effect is amplified by the high temperature and turbulent conditions present, especially in the high-velocity zones near the inlet. Considering the refractory wear induced by magnetic fluid transport and wall shear stress, optimising tundish design can lead to improved sequence life by reducing the rate of refractory wall wear. Understanding the interplay of turbulent flow, heat transfer, and electromagnetic effects within the tundish is essential to mitigate damage to the refractory lining and enhance the purity of molten steel.

Research into the channel-type induction heating tundish has largely focused on the magnetic field, characterised by its closed-loop current density, magnetic flux density distributed eccentrically along the circumference, and the asymmetric electromagnetic force across the channel's cross-section. The electromagnetic field within the channel results in an asymmetrical environment, creating rotational flows and vigorous stirring movements in the receiving and discharging chambers, which in turn impacts the temperature field, offering temperature compensation and promoting the removal of inclusions by affecting particle behaviour. Despite the consistent primary issues addressed, there has been limited exploration of certain adverse effects, such as slag-metal interactions, magneto-thermal erosion, and pinch effects. This study delves into the erosion phenomena, inclusion collision source terms, and inclusion behaviours within the tundish, varying the induction heating power. The aim is to assess the detrimental influences these factors may have on the continuous casting process during induction heating.

The article introduces an innovative approach by leveraging a multiphase coupling mathematical model to examine both the fluid dynamics and inclusion trajectories, as well as the temperature distribution within the tundish. This model also evaluates the erosion of the refractory lining triggered by the flow in real-life tundish refining processes, utilising established erosion models and a refractories wear rate factor. It examines the correlation between the average erosion rate, wear coefficient, wall shear stress, and the induction heating power. The k–ε turbulence model is employed to offer a precise depiction of the turbulent flow, and the model for inclusion concentration and mass accurately traces the path of inclusions within the tundish. Using the calculated wall shear stress and turbulence intensity, the model deduces the flow-induced erosion rate on the lining.

Physical description

Figure 1 illustrates the tundish as a hexahedral mesh representation, accompanied by its geometric shape parameters. Tables 1 and 2 detail the parameters of the physical model and the computational conditions employed. Induction heating technology is based on the principles of electromagnetic induction, where the field generator, positioned within the tundish, induces an electric current as the molten steel flows through the tundish channel. This induced current generates Joule heat, which is utilised to warm the molten steel.

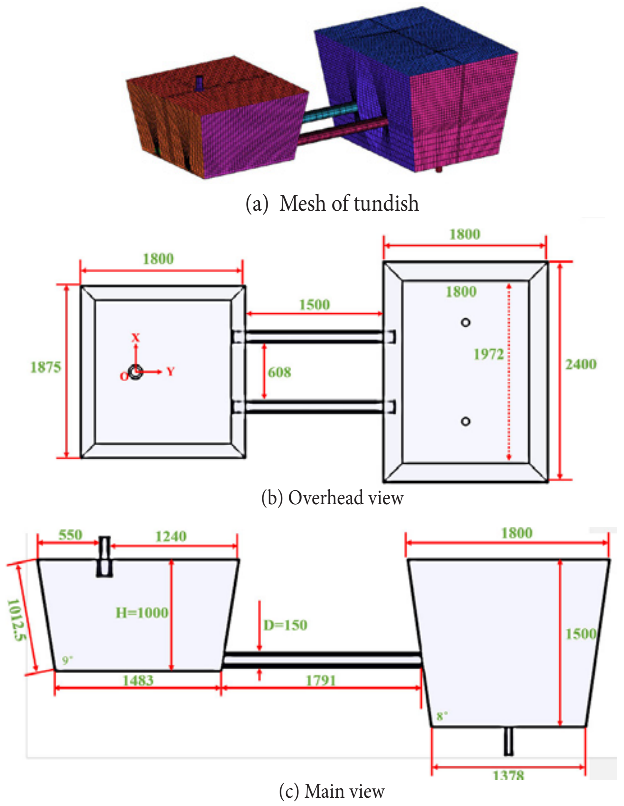

Figure 1—Hexahedral tundish mesh and geometry geometric shape of tundish

Table 1

The operating and geometry parameters of a tundish with channel type

Parameters	Value (unit)
Depth of receiving chamber	1000 mm
Depth of discharging chamber	1500 mm
Free surface size of receiving chamber	1800 mm × 1875 mm
Bottom size of receiving chamber	1558 mm × 1483 mm
Incline angle of chambers wall	9°, 8°
Diameter of channel	150 mm
Length of channel	1791 mm
Free surface size of discharging chamber	1800 mm × 2400 mm
Bottom size of discharging chamber	1972 mm ×1378 mm
Diameter of ladle shroud	100 mm
Receiving chamber volume	2.82627 m^3
Discharging chamber volume	5.2443 m^3
Tundish volume	8.131 m^3

Table 2
Calculated working conditions

Cases	Induction heating power (kW)
Case1	No
Case2	100
Case3	400
Case4	800

A secondary circulation is established by the flow of the molten steel in the tundish and its channel. When the alternating current (AC) power supply feeds the coil with its power frequency, it creates alternating magnetic flux. According to Faraday's law of electromagnetic induction, this alternating magnetic flux induces an electromotive force (F) and Joule heat (Q) within the molten steel, forming a closed circuit.

Mathematical model description

Assumptions

To manage the complexity of inclusion transport and the electromagnetism fluid coupling processes in the tundish, the following simplifying assumptions were made within the model:

- The molten steel was treated as an incompressible Newtonian fluid with temperature-dependent density, $\rho_f = 8523 - 0.8358_f$, while its other properties were considered constant.
- Inclusions were modelled as spherical entities.
- Owing to their minimal volume fraction in the liquid steel, inclusions have an insignificant impact on the overall flow pattern.
- The trajectory of an inclusion is modelled as independent until it encounters and coalesces with another.
- The chemical corrosion of the refractory materials and the chemical dynamics within the tundish were not taken into account.

The following assumptions were adopted to simplify the model due to the complicated inclusion transport phenomena and electromagnetism fluid coupling processes involved in the tundish:

Fluid flow and heat transfer

To depict the turbulent flow, the continuity and time-averaged Navier-Stokes equations were used.

$$\frac{\partial \rho_f}{\partial t} + \nabla \cdot (\rho_f \vec{u}_f) = 0 \qquad [1]$$

$$\frac{\partial(\rho_f \vec{u}_f)}{\partial t} + \nabla \cdot (\rho_f \vec{u}_f \vec{u}_f) = \nabla P + \rho_f \vec{g} + \beta(T - T_{ref})\rho_{ref}\vec{g} + \nabla \cdot [\mu_{eff}(\nabla \vec{u}_f + (\nabla \vec{u}_f)^T)] + F_E \qquad [2]$$

Where, ρ_f is the fluid density, $\vec{u}_f$ is the fluid velocity, ρ_{ref} is a reference density, P is the pressure, $\vec{g}$ is the gravitational accelerate, T is the temperature, T_{ref} is a reference temperature, F_E is the electromagnetic force, and μ_{eff} is the effective viscosity, which is defined as:

$$\mu_{eff} = \mu + \mu_t \qquad [3]$$

Where μ is the dynamic viscosity and μ_t is the turbulent viscosity.

Turbulent kinetic energy and rate of dissipation

The conventional k–ε turbulence model is employed in this paper. Equations 4 and 5 are the governing equations for turbulent kinetic energy and rate of dissipation:

$$\frac{\partial(\rho_f k)}{\partial t} + \frac{\partial(\rho_f k \vec{u}_f)}{\partial x_j} = \frac{\partial}{\partial x_j}\left[(\mu + \frac{u_t}{\sigma_k})\frac{\partial k}{\partial x_j}\right] + G_k - \rho_f \varepsilon \qquad [4]$$

$$\frac{\partial(\rho_f \varepsilon)}{\partial t} + \frac{\partial(\rho_f \varepsilon u_j)}{\partial x_j} = \frac{\partial}{\partial x_j}\left[(\mu + \frac{u_t}{\sigma_\varepsilon})\frac{\partial \varepsilon}{\partial x_j}\right] + \frac{C_{1\varepsilon}\varepsilon}{k} G_k - C_{2\varepsilon}\rho_f \frac{\varepsilon^2}{k} \qquad [5]$$

Where k is the turbulence kinetic energy, ε is the turbulent kinetic energy rate, σ_κ and σ_ε represent the Schmidt number for κ and ε, G_κ is the generation rate of turbulence energy, where C_μ, $C_{\varepsilon 1}$, $C_{\varepsilon 2}$, σ_κ, σ_ε are constants taken from Launder and Spalding.

Tracer convection-diffusion equation

To investigate the characteristics of fluid flow within a two-channel tundish, a residence time distribution (RTD) curve is generated (Yang et al., 2020). Additionally, the convection-diffusion mechanism is applied to model the transmission of tracer particles within the molten steel, as depicted in Equation 6.

$$\frac{\partial(\rho_f C_0)}{\partial t} + \nabla \cdot (\rho_f \vec{u}_f C_0) = \nabla \cdot (D_{eff} \cdot \nabla C_0) \qquad [6]$$

Where C_0 is the tracer concentration and D_{eff} is the effective kinematic diffusivity.

Thermal energy equation

The energy conservation equation should be considered as thermocouple heating (σJ^2) in the case of channel type induction heating, which is as follows:

$$\frac{\partial(\rho_f C_P T)}{\partial t} + \nabla \cdot (\rho_f T \vec{u}) = \nabla \cdot (\lambda \nabla T) + \sigma J^2 \qquad [7]$$

Where λ is the effective thermal conductivity, C_p is the heat capacity, and σ is the electrical conductivity of molten steel.

Model of inclusion collision-coalescence

Here, we propose a mathematical model that integrates the inclusion population balance with the population conservation model to describe the spatial distribution of inclusions, employing principles of mass conservation and population conservation (Lei et al., 2019).

$$\nabla \cdot (\rho_f \vec{u}_C C) = \nabla \cdot (\rho_f D_{eff,C} \nabla C) \qquad [8]$$

$$\nabla \cdot (\rho_f \vec{u}_N N) = \nabla \cdot (\rho_f D_{eff,N} \nabla N) + S_N \qquad [9]$$

The rate of inclusion generation per unit volume, represented by SN, can be positive or negative, reflecting the formation of new inclusions or the removal of existing ones. Changes in the inclusion population due to coalescence can be expressed as:

$$S_N = S_{turb} + S_{Stokes} = 2.6\alpha \left(\frac{\pi \rho_f \varepsilon}{\mu_1}\right)^{0.5} N^2 r^{*3} + \frac{10}{9\sqrt[3]{6}} \frac{\pi \vec{g} \Delta\rho}{\mu_1} N^2 r^{*4} \qquad [10]$$

$$r^* = \sqrt[3]{\frac{3C}{4\pi N}} \qquad [11]$$

Where S_N is the collision-coalescence source term, r^* is the characteristic inclusion radius, $\bar{u}_C$ is the inclusion volume concentration slipping velocity and $\bar{u}_N$ is the inclusion number density slipping velocity, C is the inclusion volume concentration, N is the inclusion number density, and μ_1 is the kinematic viscosity.

Erosion and corrosion model

Both physical and chemical erosion contribute to the degradation of the refractory liner. Physical erosion results from the movement of molten steel, while chemical corrosion ensues from high-temperature molten slag and magneto-caloric effects. Consequently, the overall wear rate is the cumulative total of erosion and corrosion rates. In this study, the erosion of the refractory liner is considered as a form of plasticity erosion, where the relative motion between the molten steel and the refractory liner generates shearing stress. Therefore, shearing stress combined with turbulence intensity could serve as predictors for estimating the rate of refractory lining erosion (Huang et al., 2013; Wang et al., 2020):

$$H_{st} = f(\tau, I) = -2.061 \times 10^{-13} (\tau \cdot I)^2 + 2.642 \times 10^{-7} (\tau \cdot I) + 5.636 \times 10^{-4} \quad [12]$$

Where, H_{st} is the erosion rate of molten steel, mm/h; τ is the shearing stress, Pa, and I is the turbulence intensity.

Refractories wear factor

A refractory wear model based on instrument wear testing was developed to forecast the wear of refractory materials in metallurgical containers. The wear rate coefficient, w, was calculated as follows (Zhang et al., 2010):

$$w = k_e \left(\frac{\tau}{\tau_0} \right)^{1/3} \quad [13]$$

Where, k_e is the effective mass transfer parameter determined by the reaction between the refractories and the molten steel. The refractory dissolving rate in molten steel can be measured to determine ke. It can be stated as a formula (Zhang et al., 2010):

$$k_e = \frac{1}{100} \exp\left[2.8956 - \left(\frac{11344}{T} \right) \right] \quad [14]$$

Where, τ is shear stress at steel-refractory interface in the tundish and τ0 is reference shear stress. Furthermore, τ_0 can be discovered through experimentation and depends on the structure and content of the refractory. The factor of refractories wear, w_0, was defined in Equation 15, in order to investigate the impact of campaign conditions on the refractories wear:

$$w_0 = w \tau_0^{1/3} = k_e \tau^{1/3} \quad [15]$$

The W_0 is a function of temperature and shear stress at steel-refractory interface. So, w0 solely refers to the campaign condition of refractories and has nothing to do with the type of refractories. The distribution of w0 in the tundish can help with refractory material selection.

Wall shear stress

$$\frac{\rho_f \bar{u}_f C_\mu^{1/4} k_p^{1/2}}{\tau_w} = \frac{1}{\varkappa} \ln \left(E \frac{\rho_f y_p C_\mu^{1/4} k_p^{1/2}}{\mu} \right) \quad [16]$$

Where, u_f is the mean velocity at the cell center adjacent to the wall, y_p is the distance from point p (adjacent to wall) to the wall, k_p is the turbulent kinetic energy at point p to the wall, k is the von Kármán constant (= 0.4187), and E is the empirical constant (= 9.793) (Singh et al., 2008).

Boundary conditions

The following boundary conditions in the tundish must be quantitatively calculated (Wang et al., 2014):

(1) At the slag surface, the normal derivatives of all variables are zero.

(2) On the tundish walls, the no-slip condition and standard wall functions are enforced, with a specified flux for non-isothermal analysis, detailed in Table 3.

(3) Employing a steady-state flow field, the inclusion collision-coalescence equation and the transient tracer advection-diffusion equation were solved to determine the inclusion concentration field and the residence time distribution (RTD) curve, respectively.

(4) The transfer of inclusions within molten steel occurs predominantly through diffusion and convection, allowing the expression of inclusion flux at the tundish boundaries (top slag, bottom wall, inclined wall, and channel wall) in terms of convection and diffusion flux (Lei et al., 2019).

The boundary conditions of flow, heat transfer, particle motion field, of which some details are shown in the Table 3, and others have been described in the paper (Lei et al., 2019; Yang et al., 2018; Yang et al., 2022; Wang et al., 2014; Yang et al., 2018).

Numerical method

A three-dimensional structured hexahedral mesh with 300,000 cells is used for numerical simulations, and grid independence is confirmed as described by (Yang et al., 2018). Computational fluid dynamics (CFD) simulations commence with the discretisation of governing equations using the CFX software to calculate the steady flow field. The transport equations are discretised via a second-order upwind scheme to yield an initial solution. The semi-implicit method for pressure-linked equations (SIMPLE) algorithm addresses pressure-velocity coupling and body forces in the momentum equation. The standard k-ε turbulence model,

Table 3

Physical parameters and boundary conditions

Parameter	Value
Free surface heat loss	8000 (W/m^2)
Bottom /wide/ narrow wall heat loss	4000 (W/m^2)
Channel wall heat loss	1800 (W/m^2)
Thermal conductivity of molten steel	41 (W/(m.K))
Heat capacity of l molten steel	750 (J/(kg.K))
Inlet temperature	1800 (K)
Density of molten steel	(8523-0.8358T) (kg/m^3)
Coefficient of thermal expansion of molten steel	0.0001 (1/K)
Viscosity of the molten steel	0.0061 (kg/(m.s))
Inlet temperature	1800 (K)
Initial inclusion volume concentration	300 ppm
Initial inclusion number density	2.65×10^{11}($1/m^3$)

combined with a second-order upwind method, models turbulence effects. Subsequent to establishing the steady-state flow field, the equations for inclusion collision-coalescence and transport are solved, tracing each inclusion's path through the flow field. Convergence is achieved when the sum of all normalised residuals for all physical variables falls below 10^{-6}.

Results and discussions

To elucidate the roles of flow erosion and magnetocaloric high-temperature erosion on refractory wall wear, simulations were conducted under a variety of conditions. The influence of the magnetic field on flow patterns dramatically varies, yielding a consistent erosion pattern on the refractory walls. Additionally, higher induction heating power correlates with increased thermal effects and consequently, more significant thermal deterioration of the refractory material. Thus, erosion, refractory wear coefficients, temperature profiles, and inclusion distributions within the induction-heated tundish are numerically forecasted across four distinct operational scenarios, as validated by (Lei et al., 2019; Yang et al., 2018; Yang et al., 2022; Yang et al., 2018).

Erosion patterns and wear coefficient distribution of refractory materials

Wall erosion in the tundish, induced by flow dynamics and channel effects, prioritises assessing the global zone where core areas impact the metallurgical vessel's lifespan. Figure 2 illustrates the rates of tundish lining wear across four operational conditions. In the absence of induction heating, the highest erosion rate occurs beneath the long nozzle at 1.172 × 10-2 mm/h and spreads circularly, diminishing from centre to periphery. This pattern ensues from high-velocity flows striking the central zone, where the intense impact translates into significant erosion at the base of the casting package. Such peak erosion exacerbates damage to the tundish refractory material.

An additional region depicted in the image distinctly presents the erosion rate at the junction between the channel and the receiving chamber. Due to its strategic positioning, substantial fluid influx into the channel renders erosion at this intersection inevitable. Erosion across the other tundish refractory linings is relatively uniform, with rates generally hovering between 1.149×10^{-2} mm/h to 1.154×10^{-2} mm/h. Concurrently, the channel lining exhibits a marginally accelerated rate of degradation compared to the tundish's sloped wall.

With the induction heating power set to 100 kW, the erosion rate and area affected by flow dynamics undergo significant alterations. Despite the erosion pattern below the long nozzle remaining largely unchanged, its intensity varies due to the electromagnetic forces at play. The peak erosion rate climbs to 1.1348×10^{-2} mm/h, owing to the enhanced agitation and concentration of the molten steel flow from the long nozzle impacting the bottom surface. This results in notably accelerated wear on the tundish's inclined wall refractory.

The addition of a magnetic field refines the fluid mixing within the tundish, inevitably leading to substantial variations in the wall lining erosion profile. With induction heating, the erosion rate rises from 1.151×10^{-2} mm/h to a range of 1.155×10^{-2} mm/h to 1.213×10^{-2} mm/h. The most pronounced increase is observed at the receiving chamber wall and its interface, where the erosion rate stabilises between 1.232×10^{-2} mm/h and 1.290×10^{-2} mm/h. There is a marked escalation in both the erosion rate and the extent of damage at this interface.

In the double-channel region, the swirling flow of the molten steel predominantly dictates the channel lining's erosion. It is notable that the erosion rate at the juncture of the receiving chamber and the channel vastly exceeds that at the discharge chamber's outlet interface. This is attributed to the former being in a dynamic inflow state, subject to continuous fluid impact, in contrast to the latter, which, being in an outflow state, does not sustain direct impactful forces.

Elevating the induction heating power to 400 kW does not shift

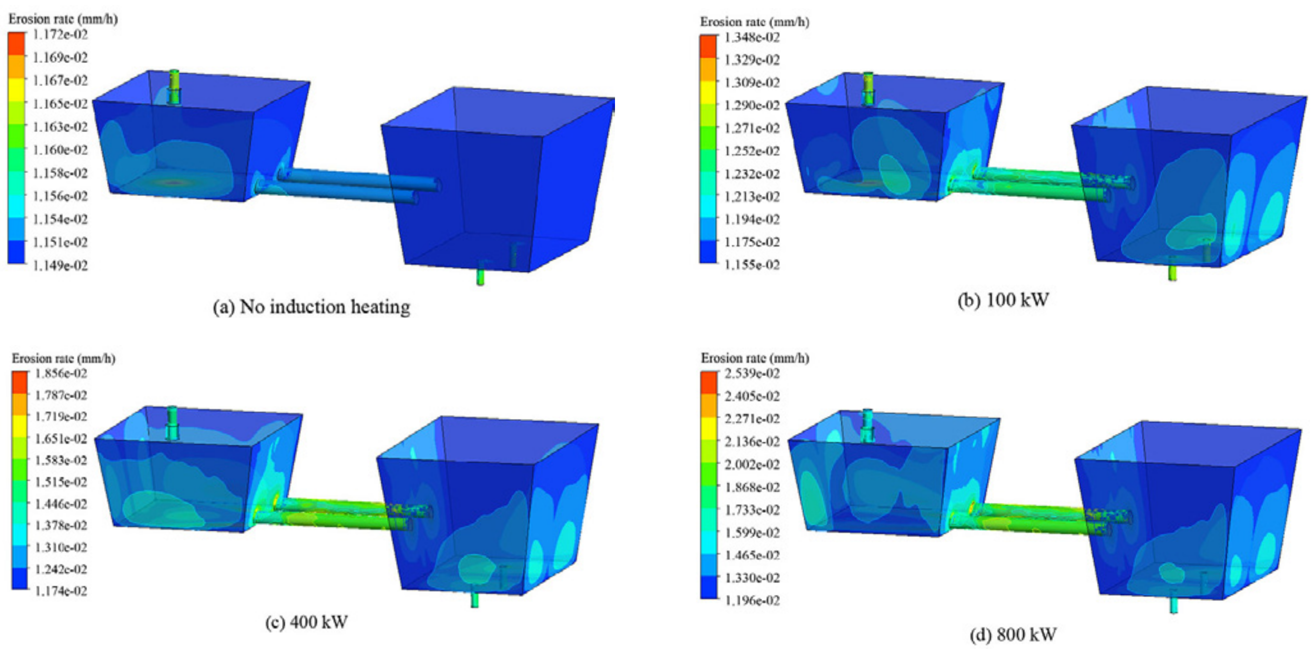

Figure 2—Distribution of flow-induced erosion rate on the refractory lining inner wall

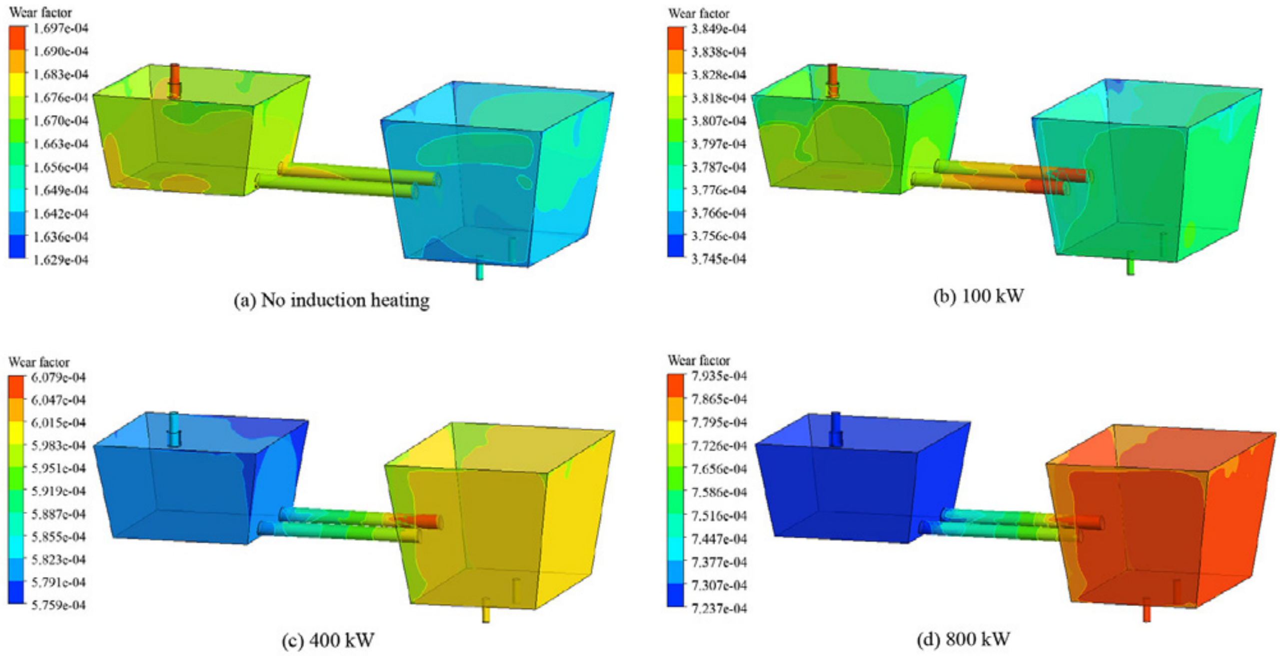

Figure 3—Refractories wear factor distribution caused by magnetocaloric induction on the inner wall of the refractory lining

the underlying erosion pattern of the tundish receiving chamber's bottom lining, yet the gradient of the erosion rate diminishes. This attenuation is primarily a consequence of the intensified electromagnetic force, which substantially modifies the molten steel's flow characteristics. Conversely, the erosion expanse of the discharging chamber's bottom lining experiences a prominent expansion. This phenomenon can be attributed to the vigorous and homogenous mixing of molten steel within the discharging chamber, combined with the steel's unidirectional egress through the outlet, continuously impacting the lining below.

As the induction heating power is ramped up, there is a corresponding gradual climb in the erosion rate of the channel lining, with figures consistently ranging between 1.446×10^{-2} mm/h to 1.651×10^{-2} mm/h. Similarly, the erosion rate of the inclined wall lining exhibits an upward trend, typically maintaining within the bounds of 1.174×10^{-2} mm/h to 1.378×10^{-2} mm/h.

Upon increasing the induction heating power to 800 kW, the erosion pattern at the bottom of the receiving chamber undergoes a marked transformation. The once circumferential gradient distribution is replaced by two symmetrical erosion surfaces, illustrating a direct correlation: the stronger the electromagnetic force, the more distinct the deviation in flow patterns and subsequent erosion impact. Meanwhile, the fundamental distribution shape of the discharging chamber's bottom lining remains unaltered, aside from variations in erosion rate. The channel lining's erosion rate consistently lies between 1.733×10^{-2} mm/h to 2.136×10^{-2} mm/h, while the inclined wall lining's rate is generally sustained between 1.196×10^{-2} mm/h to 1.733×10^{-2} mm/h.

Drawing from the preceding analysis, it is clear that an increase in induction heating power correlates with intensified erosion of the tundish lining, notably within the channel lining. While significant induction heating power does promote the homogenisation of molten steel – enhancing the heat transfer process and facilitating the agglomeration and removal of inclusions – it simultaneously precipitates vigorous erosion of the lining. Consequently, heightened erosion rates within the working zone of the lining merit focused consideration during the optimisation and design of the tundish's working lining.

Figure 3 demonstrates the wear coefficient distribution of tundish liner refractory materials under four different operational scenarios. It is evident that the wear coefficient of the refractory material escalates with the increase in induction heating power. In the absence of induction heating, the wear coefficient of refractories in the receiving chamber is considerably higher compared to that in the distribution chamber. However, with ramped-up induction heating power, the distribution chamber's refractories begin to exhibit a higher wear coefficient than those in the receiving chamber. This trend is largely attributed to the direct proportionality between the wear coefficient of refractory materials and temperature, indicating that the wear coefficient surges with rising temperatures. Notably, the peak wear coefficient of refractory materials is primarily concentrated at the channel exit due to the highest temperature and maximum Joule heat presence. The wear coefficient of refractory materials in the tundish shows a progressive increase from 1.6 × 10-4 to 3.8 × 10-4, then to 5.9 × 10-4, and finally to 7.5 × 10-4 with the induction heating power escalating from none to 800 kW.

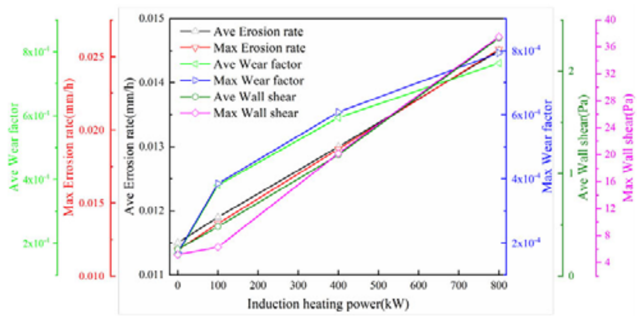

Figure 4—The characteristic of erosion rate, wear factor, and wall shear

Table 4

Mathematical models of physical parameters vs. power

Physical parameter	Fitting formula	Correlation
Avg. Erosion Rate (mm/h)	$E_{ave} = 0.01151 + 3.735 \times 10^{-6}P$	Linear positive
Avg. wear coeff. ($\times 10^{-4}$)	$W_{ave} = 7.966 \times 10^{-5}P^{0.33676}$	Power-law growth
Avg. wall shear stress (Pa)	$Save = 0.2475 + 0.00217P + 7.95 \times 10^{-8}P^2 + 5.0 \times 10^{-10}P^3$	Cubic polynomial

Hence, by understanding the distribution pattern of refractory material wear coefficients, it becomes possible to anticipate the areas or specific locations that will necessitate the use of refractories with superior wear resistance.

Figure 4 and Table 4 illustrate the progression of the erosion rate, wear coefficient, wall shear stress, and power, with maximum and average values of these three physical attributes depicted. Figure 4 indicates that these quantities exhibit an upswing as power intensifies. There is a direct correlation between the average and maximum erosion rates and average wall shear stress with power; while the other three physical properties demonstrate a nonlinear association with power, they exhibit highly predictable trends of variation. The average and maximum wear coefficients change in a nearly identical way, maintaining the same magnitude order, predominantly because the wear coefficient is primarily influenced by fluctuations in temperature.

Analysing the trends in the curves presented in Figure 4, particularly within the average physical fields, allows for the fitting of functional relationships. The correlation between the average erosion rate and power is given by $E_{ave} = 0.01151 + 3.735 \times 10^{-6}P$. The relationship between the average wear coefficient and power is modeled by $W_{ave} = 7.966 \times 10^{-5}P^{0.33676}$, and the link between average wall shear stress and power is captured by $S_{ave} = 0.2475 + 0.00217P + 7.95 \times 10^{-8}P^2 + 5.0 \times 10^{-10}P^3$. Utilising these mathematical models, the erosion rate, wear coefficient, and wall shear stress within an induction heating tundish can be accurately predicted and assessed. Consequently, this aids in effectively pinpointing the location and degree of refractory material damage within the reactor.

The data shows that the erosion rate follows a linear growth pattern (increase of 0.00037 mm/h for every 100 kW increase), and the wear coefficient follows a power law $W \propto P^{0.33676}$, reflecting the nonlinear temperature rise effect. For shear stress, it is necessary to warn of the risks carried by high-power turbulence mutations.

Table 5 shows the power-erosion-wear impact, it reveals the main core rule that although power increase improves the metallurgical process, it leads to a linear increase in erosion rate (+ 26%), and a power law increase in wear coefficient (+369%), providing a quantitative decision-making basis for the long life design of the tundish.

Variation characteristics of inclusion number density source term

During the smelting and refining process, chemical reactions lead to the creation and removal of inclusions, a dynamic captured by the volume source term Sc in the Equation 8 for inclusion mass conservation. Conversely, the fluctuation in inclusion count, driven by phenomena such as collisions and agglomeration, is articulated through the number density source term S_N in the inclusion quantity conservation Equation 10. In our computational simulations, the secondary oxidation of molten steel is disregarded, thus S_c is set to zero. Yet, while inclusion coalescence and breakage alter their number, the aggregate mass of inclusions remains unchanged. The source term for inclusion number density, SN, is essentially composed of two parts: $S_N = S_{turb} + S_{Stokes}$. By examining the spatial distribution of the source term, one can trace the shifting tendencies and governing patterns of inclusion number density within the reactor, which in turn facilitates industrial predictions, theoretical refinements, and technical enhancements of the refining process.

Figure 5 and Table 6 present the spatial distribution of the contribution of Stokes collisions to the inclusion number density source term. Insights gleaned from Figure 5 are as follows:

(1) The collision source term demonstrates its most significant impact at the entrance, diminishing progressively with the outward flow of the liquid steel.

Table 5

Power-erosion-wear impact

Power (kW)	Metallurgical benefit	Peak erosion rate ($\times 10^{-2}$ mm/h)	Avg. wear Coeff. ($\times 10^{-4}$)	High-risk zones	Protection measures
0	Low inclusion removal	1.172 (below ladle shroud)	1.6	ladle shroud impact zone	Local impact-resistant reinforcement
100	Initial steel homogenisation	1.290 (chamber-channel junction)	3.8	Receiving chamber-channel junction	Graded structure at junction
400	Improved heat transfer & inclusion removal	1.651 (channel lining)	5.9	Channel lining + distributor bottom	SiC composites at channel outlet
800	Optimal metallurgical performance	2.136 (channel lining)	7.5	1. Channel lining 2. Symmetric erosion zones	1. Flow deflector optimisation 2. Active cooling

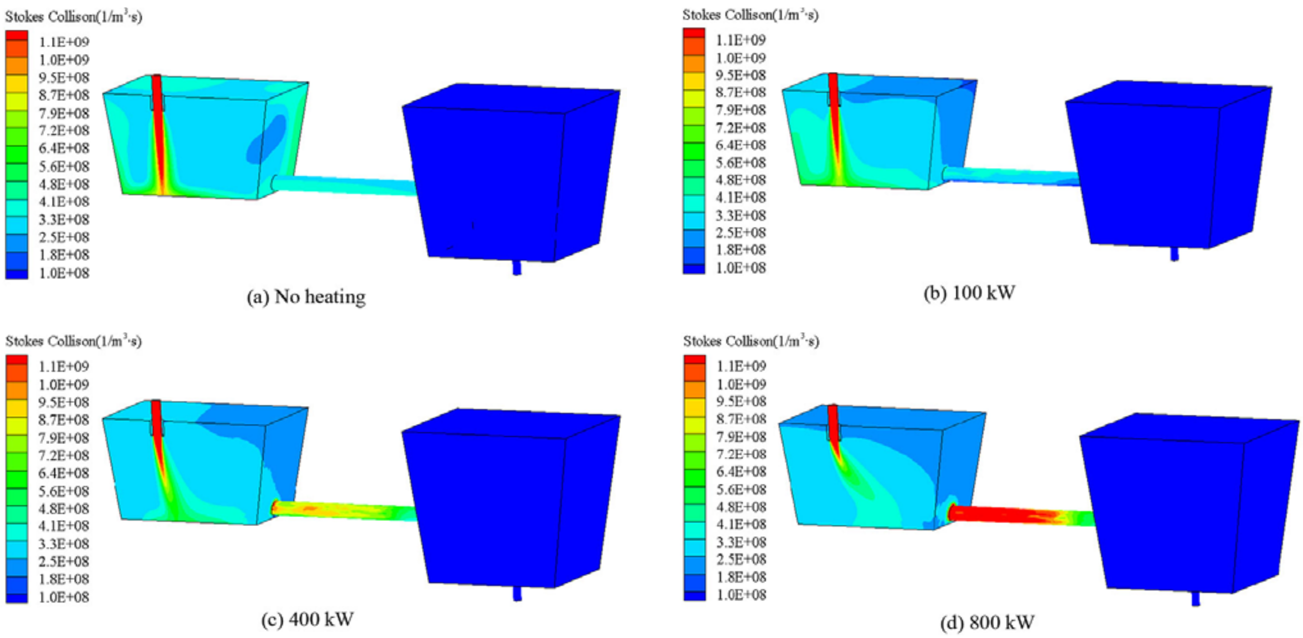

Figure 5—The spatial distribution of Stokes collision source terms

Table 6
Stokes collision source distribution features

Region	0 kW (1/m³·s)	100 kW (1/m³·s)	400 kW (1/m³·s)	800 kW (1/m³·s)	Variation pattern
Inlet zone	Peak area	Distribution shift	Enhanced shift	Significant shift	EM force alters steel flow direction
Channel	3.3×10^8~4.1×10^8	3.3×10^8	5.6×10^8~8.7×10^8	1.1×10^9	Sharp 233% increase (0→800 kW)
Chamber + Channel	>95% total contribution	>95%	>95%	>95%	Core collision zone (dominant)
Distributor	≈1×10^8	≈1×10^8	≈1×10^8	≈1×10^8	Stable low (velocity drop reduces collision)
Channel outlet	Collision drop zone	Collision drop	Collision drop	Collision drop	Rapid velocity decrease lowers collision probability

(2) With an uptick in heating power, there is a noticeable shift in the distribution of the collision source term's contribution at the inlet. This shift occurs because increased power intensifies the electromagnetic stirring force, altering the flow trajectory of steel from the inlet towards the bottom, such that it is no longer strictly perpendicular.

(3) In the absence of induction heating, the contribution gradient of the inclusion number density collision source term in the channel remains modest, hovering between 3.3×10^8(1/m³·s) and 4.1 × 108 (1/m³·s). However, upon the application of induction heating, as the heating power surges from 100 kW to 800 kW, the contribution of this collision source term escalates dramatically from 3.3×10^8 (1/m³·s) to 1.1×10^9 (1/m³·s), signifying a substantial tenfold increase.

(4) The receiving chamber and the channel together constitute over 95% of the Stokes collision contribution concerning inclusions within the tundish. The collision contribution within the distribution chamber largely stabilizes at 1×10^8 (1/m³·s), underscoring the discharging chamber and channel as pivotal zones for Stokes collisions. This is primarily due to the drastic reduction in velocity of molten steel as it exits the channel outlet, resulting in a marked decrease in the collision source contribution.

(5) An increase in heating power corresponds to a higher contribution from the Stokes collision density source term in the channel. This is largely attributable to the augmented pinch force exerted on the molten steel within the channel, which intensifies in tandem with the rising electromagnetic force.

Figure 6 and Table 7 show the spatial distribution and feature of the contribution of turbulent collision to the inclusion number density source term. It can be seen that its distribution is significantly different from the spatial distribution of the Stokes collision contribution to the inclusion number density source term. Its characteristics are as follows:

(1) The magnitude of the source term of the inclusion number density caused by turbulent collision is basically maintained at 1×10^6~3×10^8 (1/m³·s), which is significantly smaller than the contribution of the Stokes collision source term.

(2) As the induction heating increases, the contribution of the

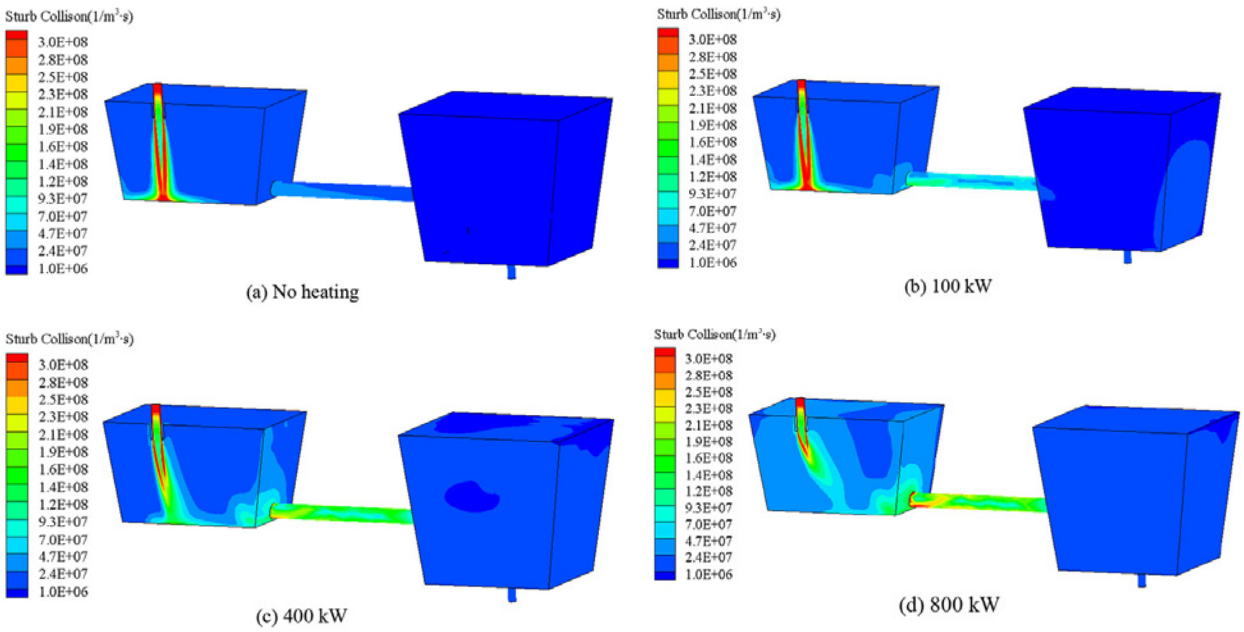

Figure 6—The spatial distribution of turbulent collision source terms

Table 7

Turbulent collision source distribution features

Parameter	Value range (1/m³·s)	Power impact	Spatial feature	vs. Stokes collision
Overall magnitude	1×10^6~3×10^8	Increases with power	Distribution differs from Stokes	1-2 orders lower
Channel zone	1×10^6~3×10^8	Significant increase (turbulent kinetic energy ↑)	EM force boosts turbulence	Lower sensitivity than Stokes
Vertical inlet	Peak zone	Large EM-induced deflection	Steepest gradient change	Consistent trend with Stokes
Other regions	Low-value zone	Minor increase	Relatively uniform distribution	Similar contribution magnitude

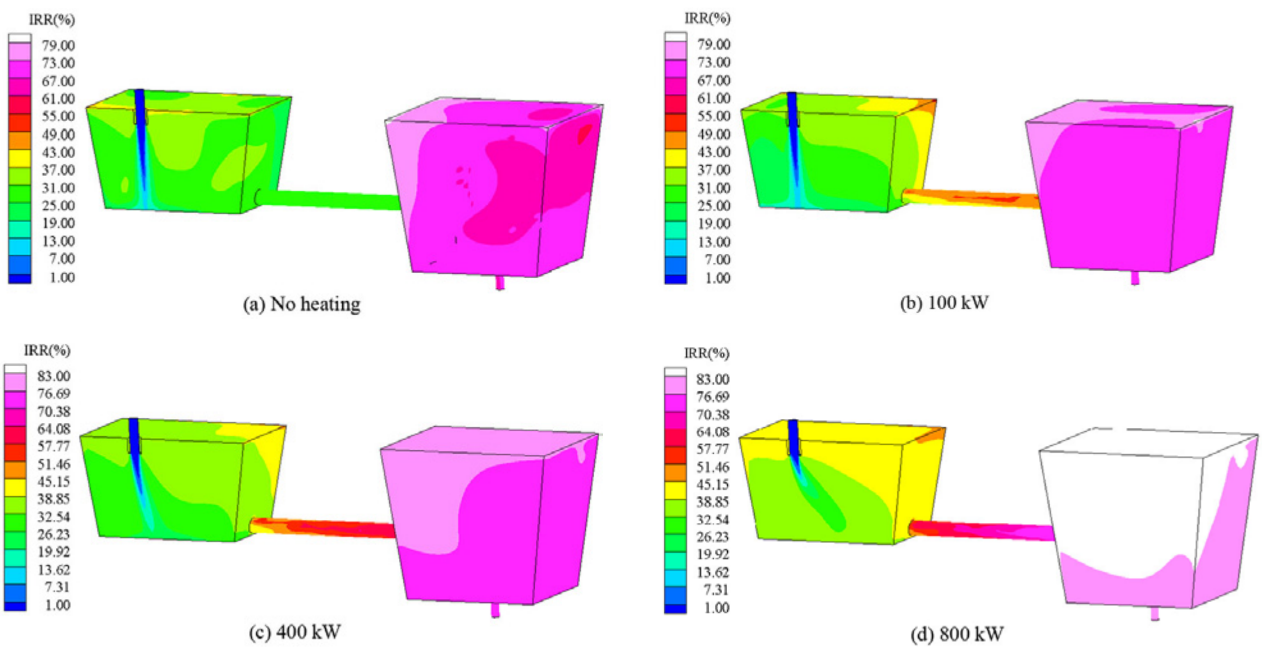

Figure 7—Spatial distribution of inclusion removal rates

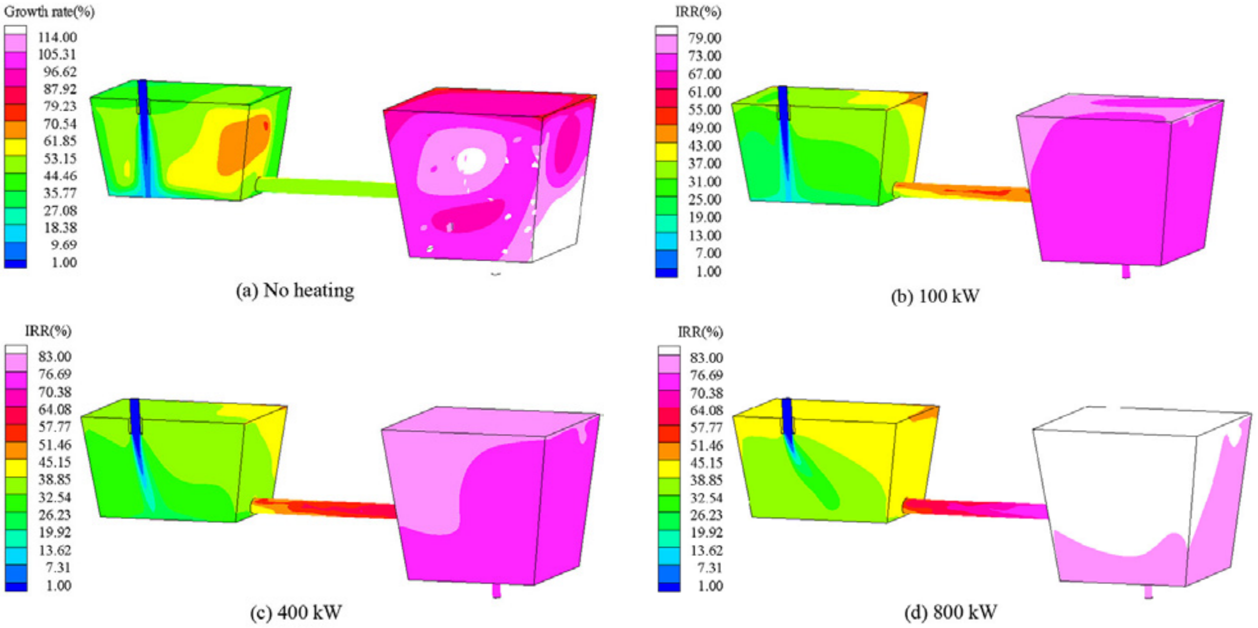

Figure 8—Spatial distribution of inclusion growth rate

collision source term at the channel increases significantly. This is because the electromagnetic force significantly increases the turbulent kinetic energy in the channel. Collision source terms in other areas will also increase, but the increase is relatively small.

(3) The collision in the vertical direction of the entrance is the most obvious, and the gradient change is also the largest. Its change is consistent with the Stokes collision source term. It is affected by the electromagnetic force and undergoes a large deflection.

In summary, induction heating can effectively increase the contribution of collision to the source term of inclusion number density, and the greater the power, the greater the contribution, which means that the collision rate of inclusions is accelerated, the particle size change gradient is large, and inclusion removal will also be improved.

Spatial distribution characteristics of inclusion field features

Figure 7 depicts the spatial distribution of the characteristic inclusion removal rates in the midsection under four operational scenarios. In the absence of induction heating, the inclusion removal rate in the receiving chamber stabilises at around 25%. As the fluid traverses the channel, this rate remains largely constant, illustrating that without induction heating, the channel's role in inclusion removal is minimal, functioning primarily as a conduit for fluid flow. Upon entering the discharging chamber, the removal rate ascends to approximately 70%.

When the induction heating power reaches 100 kW, there is a marked shift in the gradient of the inclusion removal rate within the receiving chamber, particularly at the corners near the slag surface; here, the rate peaks at 50%, with the removal at the slag surface substantially surpassing that of its inner regions. Compared to the scenario without induction heating, the inclusion removal rate within the channel has notably increased, and the gradient variation in the discharging chamber has lessened. This is attributed to the electromagnetic force's influence, where the majority of inclusions are eliminated within the receiving chamber and channel, thereby diminishing the inclusion removal in the discharging chamber and reducing its capacity for removal.

With induction heating powers set at 400 kW and 800 kW, the inclusion removal rates in the discharging chamber surge to 40%, representing a significant enhancement, while the channel's removal rate climbs to 60%. Furthermore, there is an upturn in the gradient of the inclusion removal rate within the channel. As for the distribution chamber, the removal rate is consistently maintained at around 80%, with a more subdued gradient in the inclusion removal rate.

Figure 8 illustrates the spatial distribution of inclusion growth rates within the tundish across four operational conditions. In the absence of induction heating, the growth rate intensifies progressively from the receiving to the discharging chamber, with inclusion particle size reaching its maximum in the discharging chamber. As induction heating power increases from 100 kW to 800 kW, the total inclusion growth rate decreases markedly from 76% to 28%, and specifically within the discharging chamber, the rate descends from 70% to 20%, with a concomitant decline in the gradient. This pattern indicates that a higher induction heating power correlates with an expedited removal of inclusions, leading to a significant reduction of large-sized inclusions before their transit into the discharging chamber.

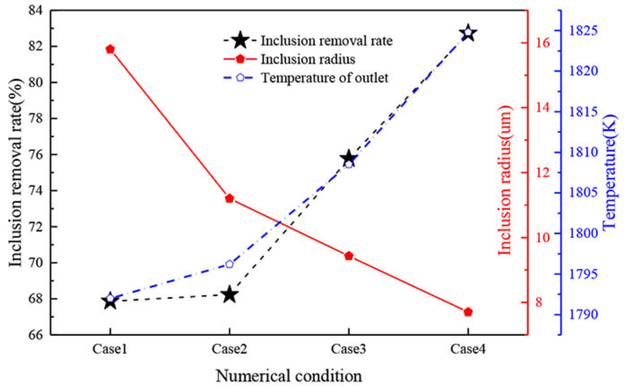

Figure 9—Multiple physics of tundish outlet

Table 8
Power-driven refining efficiency enhancement

Power comparison	Removal rate ↑	Particle size ↓	Temp. Rise (K)	Core benefit
0→100 kW	+0.36%	-4.6 μm (-29.1%)	+4.2	Minor improvement
100→400 kW	+7.54%	-1.77 μm (-15.8%)	+12.3	Significant size distribution optimisation
400→800 kW	+6.96%	-1.73 μm (-18.3%)	+16.3	Revolutionary refining enhancement
0→800 kW	+14.86%	-8.1 μm (-51.3%)	+32.8	Full optimisation: removal ↑ + size ↓ + temp. control ↑

Figure 9 presents the variations in inclusion removal rate, radius, and temperature correlating with power at the tundish outlet across four distinct operational scenarios. With the sole exception of the state without induction heating, there exists a linear relationship function that ties together the inclusion removal rate, inclusion radius, outlet temperature, and the power of induction heating. This linear function provides a reliable prediction of the physical field for a specific magnitude. The inclusion removal rates for the four respective conditions are 67.87%, 68.23%, 75.77%, and 82.73%. As indicated, the impact of low power on enhancing inclusion removal is negligible, with a mere 0.36% increase in removal rate when escalating from the absence of induction heating to 100 kW. The liquid steel temperatures at the outlets for these conditions are 1792 K, 1796.2 K, 1808.5 K, and 1824.8 K. Notably, at 100 kW, the outlet temperature remains 3.8 K lower than the inlet. This provides a reference for the apt selection of induction heating power corresponding to diverse operational scenarios. Inclusion particle sizes at the tundish exit under these conditions measure at 15.8 um, 11.2 um, 9.43 um, and 7.7 um, demonstrating that the electromagnetic field effectively reduces the inclusion particle size in the continuous casting billet.

The inclusion particle sizes measured at the tundish outlet across the four operational states are 15.8 μm, 11.2 μm, 9.43 μm, and 7.7 μm, respectively. This trend signifies the effectiveness of the electromagnetic field in reducing inclusion particle sizes within the continuous casting billet.

Table 8 shows that EM forces achieve synergistic refining via collision efficiency (Sec. 4.2) and flow optimisation, realising "removal ↑ + size ↓". Peak efficiency is at 800 kW. Furthermore, 400 kW is the efficiency tipping point for cost-effective refining and 800 kW maximises quality (removal rate ↑, size ↓) but intensifies refractory erosion. Particle size control dominates low-power stages, while removal rate drives high-power benefits.

Conclusion

(1) An increase of 100 kW in induction heating power linearly raises the average erosion rate by 0.00037 mm/h. The channel lining experiences the most severe erosion, reaching 2.136×10^{-2} mm/h at 800 kW.

(2) The refractory wear coefficient follows a power-law relationship with power ($W \propto P^{0.33676}$), attaining 7.5×10^{-4} at 800 kW—a 369% increase versus no-heating conditions.

(3) At high power (800 kW), the Stokes collision source term intensity in the channel surges to 1.1×10^{9} $m^{-3} \cdot s^{-1}$, marking a 233% increase compared to unheated operations and accelerating inclusion agglomeration.

(4) At 800 kW, the inclusion removal rate rises to 82.73% with a reduced outlet average particle size of 7.7 μm. Notably, 400 kW represents the cost-effective tipping point (removal rate: 75.77%).

(5) While high power improves steel cleanliness and temperature homogeneity, it intensifies refractory erosion. This necessitates balancing strategies such as local reinforcement (e.g., SiC composites at channel exits) or flow-field optimisation.

Acknowledgement

We thank the Fundamental Research Funds for the Liaoning Universities (LJ212410146002) and the University of Science Technology of Liaoning United Fund (HGSKL-USTLN(2022)07), Project supported by the Natural Science Foundation of Liaoning Province, China (Grant No.2024-BS-219), and the National Natural Science Foundation of China (Grant NO.NSFC52074151) as well as the Education Department Project of Liaoning Province (Grant NO.2020LNJC03), and the Department of Science & Technology of Liaoning Province (Grant NO.2022JH2/101300079) for the financial support of the current work.

Conflict of interest

The authors declare no conflict of interest.

References

Bao, Y.P., Wang, M. 2021. *Development trend of tundish metallurgical technology*. Continuous Casting, vol. 40, no. 5. pp. 2–11.

Blond, E., Schmitt, N., Hild, F., Blumenfeld, P., Poirier, J. 2007. *Effect of slag impregnation on thermal degradations in refractories. Journal of the American Ceramic Society*, vol. 90. pp. 154–161.

Crudu, I., Ionescu, M.P., Munteanu, V., Sandu, I.F., Nedelcu, P. 1998. *A tribosystemic approach to refractory lining destruction in blast furnaces*. Wear, vol. 216, no. 2. pp. 251–261.

Ghojel, J.I., Ibrahim, R.N. 2004. *Computer simulation of the thermal regime of double loop channel induction furnaces. Journal of Materials Processing Technology*, vol. 153–154. pp. 386–391.

Huang, A.O., Gu, H., Zhang, M., et al. 2013. *Mathematical Modeling on Erosion Characteristics of Refining Ladle Lining with Application of Purging Plug*. Metallurgical and Materials Transactions B, vol. 44, no. 3. pp. 744–749.

Lei, H., Yang, B., BI, Q., Xiao, Y.Y., Chen, S.F., Ding, C.Y. 2019. *Numerical simulation of collision coalescence and removal of inclusion in tundish with channel type induction heating*. ISIJ International, vol. 59. pp. 1811–1819.

Lian, P., Huang, A., Gu, H., et al. 2018. *Towards prediction of local corrosion on alumina refractories driven by Marangoni convection*. Ceramics International, vol. 44, no. 2. pp. 1675–1682.

Pan, D., Guo, Q.T., Yu, F.Z., Xiao, Y.B. 2022. *Research and Application Progress of Tundish Electromagnetic Induction Heating Technology*. Continuous Casting, vol. 41, no. 2. pp. 2–7.

Rovnushkin, V.A., Visloguzova, E.A., Spirin, S.A., Shekhovtsov, E.V., Kromm, V.V., Metelkin, A.A. 2005. *Composition of ladle slag and refractory materials and its effect on the wear resistance of the lining of an rh vacuum degasser*. Refractories and Industrial Ceramics, vol. 46, no. 3. pp. 193–196.

Sheng, D.Y. 2022. *Mean Age Theory in Continuous Casting Tundish*. Metallurgical and Materials Transactions B, vol. 53. pp. 2735–2752.

Singh, V., Pal, A.R., Panigrahi, P. 2008. *Numerical simulation of flow induced wall shear stress to study a curved shape billet caster tundish design*. ISIJ International, vol. 48, no. 4. pp. 430–437.

Tang, H.Y., Liu J.W., Wang, K.M., Xiao, H., Li, A.W., Wang, J.Q. 2021. Hydrodynamic modeling and mathematical simulation on flow field and inclusion removal in a seven-strand continuous casting tundish with channel type induction heating. *Acta Metallurgica Sinica*, vol. 57. pp. 1229–1240.

Wang, Q., Jia, S., Qi, F., et al. 2020. *A CFD Study on Refractory Wear in RH Degassing Process*. ISIJ International, vol. 60, no. 9. pp. 1938–1947.

Wang, Q., Qi, F.S., Li, B.K., Tsukihashi, F. 2014. *Behavior of non metallic inclusions in a continuous casting tundish with channel type induction heating*. ISIJ International, vol. 54, no. 12. pp. 2796–2805.

Wang, Y., Zhao, M.J., Yang, S.F., Li, J.S., Zhang, G.X., Xi, X.J. 2020. *Physical simulation of plasma heating in tundish*. Chinese Journal of Engineering, vol. 42, no. z1. pp. 68–73.

Wei, G., Jiang, Z.H., Zhan, D.P., Yang, X.Y. 2012. *Research on induction heating apparatus of tundish*. Journal of Iron and Steel Research International, vol. S2. pp. 726–730.

Xie, W.X., Bao, Y.P., Wang, M., Zhang, L.Q. 2014. *Application of Induction Heating Liquid in a 30 t Tundish in Continuous Casting Production of Special Steels*. Special Steel, vol. 35, no. 6. pp. 28–31.

Xing, F., Zheng, S.G., Zhu, M.Y. 2018. *Motion and removal of inclusions in new induction heating tundish*. Steel Research International, vol. 89. https://doi.org/10.1002/srin.201700542

Yong, W., Zhao, M.J., Yang, S.F., Li, J.S., Zhang, G.X., Xi, X.J. 2020. Physical simulation of plasma heating in tundish. *Chinese Journal of Engineering*, vol. 42, no. z1. pp. 68–73.

Yang, B., Deng, A.Y., Kang, X.L., Duan, P.F., Wang, E.G. 2022. *Numerical Study on the influence of distributing chamber volume on metallurgical effects in two strand induction heating tundish*. Metals, vol. 12, no. 3. https://doi.org/10.3390/met12030509

Yang, B., Lei, H., Bi, Q., Jiang, J.M., Zhang, H.W., Zhao, Y., Zhou, J.A. 2018. *Fluid flow and heat transfer in a tundish with channel type induction heating*. Steel Research International, vol. 89. https://doi.org/10.1002/srin.201800173

Yang, B., Lei, H., Bi, Q., Jiang, J.M., Zhang, H.W., Zhao, Y., Zhou, J.A. 2018. *Electromagnetic conditions in a tundish with channel type induction heating*. Steel Research International, vol. 89, no. 10. https://doi.org/10.1002/srin.201800145

Yang, B., Liao, X.W., Liu, K., Zhao, C.L., Han, P. 2022. *Numerical simulation of residence time distribution (RTD) in tundish with channel type induction heating*. JOM, vol. 74, no. 5. pp. 2129–2138.

Zhang, M.J., Lin, X.L., Yan, W., et al. 2010. *Numerical Simulation of Flow Induced Corrosion in One Strand Tundish*. Advanced Materials Research, vol. 105–106. pp. 142–145.

Zhao, M.J., Wang, Y., Yang, S.F., Li, J.S., Liu, W., Song, Z.Q. 2021. *Flow behavior and heat transfer of molten steel in a two strand tundish heated by plasma*. Journal of Materials Research and Technology, vol. 13. pp. 561–572. ◆